J. Fluid Mech. (1998), *vol.* 357, *pp.* 123–140. Printed in the United Kingdom

Stability of the flow of a fluid through a flexible tube at intermediate Reynolds number

By V. KUMARAN

Department of Chemical Engineering, Indian Institute of Science, Bangalore 560 012, India

(Received 4 June 1996 and in revised form 13 August 1997)

The stability of the flow of a fluid in a flexible tube is analysed over a range of Reynolds numbers $1 < Re < 10^4$ using a linear stability analysis. The system consists of a Hagen–Poiseuille flow of a Newtonian fluid of density ρ, viscosity η and maximum velocity V through a tube of radius R which is surrounded by an incompressible viscoelastic solid of density ρ, shear modulus G and viscosity η_s in the region $R < r < HR$. In the intermediate Reynolds number regime, the stability depends on the Reynolds number $Re = \rho VR/\eta$, a dimensionless parameter $\Sigma = \rho GR^2/\eta^2$, the ratio of viscosities $\eta_r = \eta_s/\eta$, the ratio of radii H and the wavenumber of the perturbations k. The neutral stability curves are obtained by numerical continuation using the analytical solutions obtained in the zero Reynolds number limit as the starting guess. For $\eta_r = 0$, the flow becomes unstable when the Reynolds number exceeds a critical value Re_c, and the critical Reynolds number increases with an increase in Σ. In the limit of high Reynolds number, it is found that $Re_c \propto \Sigma^{\alpha}$, where α varies between 0.7 and 0.75 for H between 1.1 and 10.0. An analysis of the flow structure indicates that the viscous stresses are confined to a boundary layer of thickness $Re^{-1/3}$ for $Re \gg 1$, and the shear stress, scaled by $\eta V/R$, increases as $Re^{1/3}$. However, no simple scaling law is observed for the normal stress even at $10^3 < Re < 10^5$, and consequently the critical Reynolds number also does not follow a simple scaling relation. The effect of variation of η_r on the stability is analysed, and it is found that a variation in η_r could qualitatively alter the stability characteristics. At relatively low values of Σ (about 10^2), the system could become unstable at all values of η_r, but at relatively high values of Σ (greater than about 10^4), an instability is observed only when the viscosity ratio is below a maximum value η^*_{rm}.

1. Introduction

Many biological systems and biotechnology processes involve flow through flexible tubes and channels. The flow of blood and other fluids in the body takes place through flexible tubes, and the separation and purification processes in pharmaceutical industries often involve flow in tubes and channels made up of polymer matrices and membranes. These have been analysed using models similar to those for the flow in a rigid tube, but some experiments conducted by Krindel & Silberberg (1979) suggest that the characteristics of the flow in a flexible tube could be very different. In the present analysis, the stability of the flow in a flexible tube is analysed in the Reynolds number range from 1 to 10^4 for various fluid and wall parameters. This work complements the earlier asymptotic analyses of the author (Kumaran 1995*a*, *b*) in the low and high Reynolds number regimes, and provides the transition

characteristics in the intermediate Reynolds number regime which is appropriate for blood flows and the experiments of Krindel & Silberberg (1979).

There has been considerable work done on the instability leading to the collapse of a flexible tube due to the difference between the internal and external pressures. This has physiological applications related to the flow of air in the respiratory passages. Detailed experiments have been conducted by Bertram (1986) on the different types of oscillatory behaviour, and the transitions between these have been characterized by Bertram, Raymond & Pedley (1989). There have also been other theoretical studies in this area by Reyn (1987), Jensen & Pedley (1989) and others. In these studies, the flow is in the turbulent regime, and the cross-sectional area of the tube is related to the difference between the external and internal pressure. The present analysis is qualitatively different from these studies, because the base flow is laminar, and the instability of the laminar flow in a tube with viscoelastic walls is examined. The instability leads to oscillations of the walls and a modification of the flow, but does not result in a significant change in the tube geometry.

The stability of the flow through a rigid tube has been examined using asymptotic analysis by Corcos & Sellars (1959) and Gill (1965). These studies found that both the centre and wall modes are always damped, and there are no unstable modes in the high Reynolds number limit. There have been many linear stability analyses of the Hagen–Poiseuille flow to axisymmetric and non-axisymmetric disturbances at finite Reynolds number (Davey & Drazin 1969; Garg & Rouleau 1972; Salwen & Grosch 1972). These have all concluded that the flow is stable to small disturbances at all Reynolds numbers, and there now appears to be a consensus that the flow in a rigid tube is stable to small-amplitude perturbations, but the observed instability may be due to perturbations of finite amplitude. The flow in a flexible tube is qualitatively different from that in a rigid tube in both the low and high Reynolds number limits.

The stability of the 'viscous modes' in the flow through a flexible tube was analysed by Kumaran (1995*a*). The analysis indicated that the fluctuations could become unstable when the velocity is increased beyond a critical value. The instability is caused by the transport of energy from the mean flow to the fluctuations due to the shear work done by the mean flow at the interface. The stability of the 'inviscid modes' in the high Reynolds number limit was considered in Kumaran (1995*b*, 1996). In this case, the flow is inviscid in the core of the tube, and there is a wall layer of thickness $O(Re^{-1/2})$ smaller than the tube radius where the viscous stresses are $O(Re^{-1/2})$ smaller than the inertial stresses. An asymptotic analysis in the small parameter $\epsilon = Re^{-1}$ was used, and in the leading approximation the real part of the growth rate is zero, indicating that the perturbations are neutrally stable at this level of approximation. The $O(\epsilon^{1/2})$ correction to the growth rate due to the stresses in the wall layer turns out to be negative. This is because the transport of energy from the mean flow to the fluctuations due to the shear work is equal in magnitude and opposite in direction to that due to the convective terms in the momentum equation, and there is a small stabilizing effect due to the viscous dissipation in the wall layer.

The low Reynolds number analysis showed that the fluid flow could become unstable when the dimensionless velocity is increased beyond a critical value, but the high Reynolds number analysis indicated that the inviscid modes are always stable. In § 2, the stability of the flow in the intermediate Reynolds number regime $1 \leqslant Re \leqslant 10^4$ is analysed using a linear stability analysis. Though attention is restricted to axisymmetric modes, it is expected that the behaviour of non-axisymmetric modes will be qualitatively similar for the following reason. The results indicate that the vorticity in the fluid is restricted to a boundary layer of thickness $Re^{-1/3}$ at the wall,

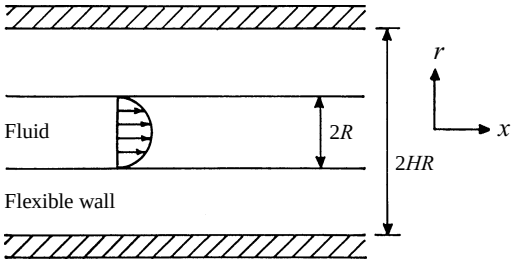

FIGURE 1. Configuration and coordinate system used for the analysis.

and the leading-order viscous stress is due to the normal variation of the tangential velocity at the wall. It is expected that the fluid velocity profile will be qualitatively similar for non-axisymmetric disturbances, since the length scale in the polar direction, which is the tube radius, is large compared to the boundary layer thickness. The details of the analysis are given in § 2, and the conclusions are summarized in § 3.

2. Analysis

2.1. *Equations of motion*

The configuration consists of a Newtonian fluid of density ρ and viscosity η flowing through a tube of radius R surrounded by a viscoelastic solid with density ρ, viscosity η_s and coefficient of elasticity G in the annular region $1 < r < H$ as shown in figure 1. Here, r and x are the radial and axial coordinates scaled by the tube radius R. In this section, the lengths are scaled by R, the time by η/G and the velocity by GR/η, these being the natural scales in the low Reynolds number limit. The mean flow in the fluid has a parabolic velocity profile:

$$\bar{v}_x = \Gamma(1 - r^2), \tag{2.1}$$

where $\Gamma = V\eta/GR$ is the scaled maximum velocity in the fluid. The non-dimensional Navier–Stokes equations for the fluid are

$$\partial_i v_i = 0, \tag{2.2}$$

$$(Re/\Gamma)(\partial_t + v_j\partial_j)v_i = -\partial_i p + \partial_j^2 v_i, \tag{2.3}$$

where the subscripts i and j represent the components of a vector, repeated subscripts represent dot products, $\partial_t \equiv \partial/\partial t$ and $\partial_i \equiv \partial/\partial x_i$. In (2.2) and (2.3), v_i and p are the velocity and pressure fields scaled by GR/η and G respectively, and $Re = \rho VR/\eta$ is the Reynolds number based on the maximum fluid velocity. The stress tensor for the fluid, scaled by G, is

$$\tau_{ij} = -p\delta_{ij} + (\partial_i v_j + \partial_j v_i). \tag{2.4}$$

The equations used for the wall material are those for an incompressible elastic solid (Landau & Lifshitz 1989) modified to include viscous effects (Kumaran 1993, 1995*a*, *b*). The dynamics of the solid is described by the displacement field u_i, scaled by the radius of the tube R, which is the displacement of the material points from their equilibrium positions due to the fluid stresses. In an incompressible solid, the displacement field satisfies the solenoidal condition

$$\partial_i u_i = 0, \tag{2.5}$$

while the momentum conservation equation is

$$(Re/\Gamma)\partial_t^2 u_i = -\partial_i p + \partial_j^2 u_i + \eta_r \partial_j^2(\partial_t u_i), \tag{2.6}$$

where $\eta_r = (\eta_s/\eta)$ is the ratio of the viscosities of the solid and fluid. The first term on the right-hand side is the gradient of the pressure required to satisfy incompressibility, the second is the divergence of an elastic stress due to the strain in the wall medium while the third term is the divergence of a viscous stress. The stress tensor for the solid, scaled by G, is

$$\sigma_{ij} = -p\delta_{ij} + (1 + \eta_r \partial_t)(\partial_i u_j + \partial_j u_i). \tag{2.7}$$

The above form for the momentum equation and the stress tensor, incorporating frequency-independent coefficients of elasticity and viscosity, have been used by Harden, Pleiner & Pincus (1991) and Kumaran (1993) to describe the surface fluctuations on polymer gels, and in the previous stability analyses of Kumaran (1995*a*, *b*). Experimental studies have reported that the storage modulus for polymer gels does have a constant 'plateau value' over the frequency range 10^{-2} to 10^3 s^{-1}, (Tong & Liu 1993), and so the assumption regarding the frequency-independent elasticity is a good one. (The terms 'storage modulus' and 'loss modulus' refer to the real and imaginary parts of the shear modulus.) Moreover, Krindel & Silberberg (1979) reported that their experiments were carried out in a range of frequencies where a plateau exists for the storage modulus. However, they did not provide any information about the loss modulus, so in the present analysis we use the simplest approximation, where the viscosity is considered independent of the frequency. The neutral stability curves obtained in the present analysis can easily be extended to a system with frequency-dependent viscosity. For a system with viscosity $\eta_r'(\omega)$ dependent on the frequency ω, the critical value of $\eta_{rc}'(\omega)$ for neutrally stable modes is related to the critical value η_{rc} determined in the present analysis for frequency-independent viscosity by the relation $\eta_{rc}'(\omega_c) = \eta_{rc}$, where ω_c is the frequency of the neutrally stable modes in the present analysis.

The boundary conditions at the interface between the solid and the fluid are the continuity of velocity and stress:

$$v_i = \partial_t u_i, \quad \tau_{ij} = \sigma_{ij}. \tag{2.8}$$

In the linear analysis, small-amplitude axisymmetric normal mode perturbations are placed on the fluid velocity field and the displacement field in the solid of the form

$$v_i = \bar{v}(r)\delta_{ix} + \tilde{v}_i(r)\exp(\mathrm{i}kx + st), \quad u_i = \tilde{u}_i(r)\exp(\mathrm{i}kx + st), \tag{2.9}$$

where $\bar{v}(r)$ is the mean velocity, x is the axial coordinate, k is a real wavenumber and s is a complex growth rate in the temporal stability analysis. In the linear analysis, the growth rate is affected by the mean velocity profile due to the convective term in the conservation equation, but is not affected by the mean pressure and stress fields because there are no nonlinear terms involving these fields in the conservation equation. In addition, both the shear and normal stresses as well as their gradients are continuous across the interface between the fluid and the wall (see Kumaran 1995*a*), and so the boundary conditions for the perturbations to the pressure and stress fields do not contain terms proportional to the mean pressure or stress. The mean pressure gradient along the tube causes a variation in the radius of the tube, which in turn could affect the mean flow. However, in the experiments of Krindel & Silberberg (1979), the variation in the tube radius was found to be small, and it was estimated

in Kumaran (1995*a*) that the slope of the tube wall is $O(10^{-3})$. Consequently, the variation in the radius of the tube is neglected in the present analysis, and the tube is considered to be of constant diameter.

The linearized mass and momentum equations for the fluid can be reduced to a fourth-order equation for the radial velocity $\tilde{v}_r$:

$$[-(Re/\Gamma)(s+\Gamma ik(1-r^2))+d_r^2+r^{-1}d_r-r^{-2}-k^2](d_r^2+r^{-1}d_r-r^{-2}-k^2)\tilde{v}_r=0, \quad (2.10)$$

and the linearized mass and momentum equations for the wall material can be reduced to a fourth-order equation for the displacement field $\tilde{u}_r$ in the wall:

$$[-(Re/\Gamma)s^2+(1+\eta_r s)(d_r^2+r^{-1}d_r-r^{-2}-k^2)](d_r^2+r^{-1}d_r-r^{-2}-k^2)\tilde{u}_r=0, \quad (2.11)$$

where $\mathrm{d}_r \equiv (\mathrm{d}/\mathrm{d}r)$. The boundary conditions for the solid are the zero-displacement conditions $\tilde{u}_r = 0$ and $\tilde{u}_x = 0$ at the outer surface $r = H$. At the interface between the fluid and the wall, it is necessary to apply the mass and momentum balance conditions. In the linear analysis, the velocity and stress fields due to the mean flow and the perturbations at the perturbed interface are expanded in a Taylor series about their values at the unperturbed interface at $r = 1$. The linear terms in the series expansion are retained and the higher-order terms are neglected to obtain the following conditions in which all the quantities are evaluated at the unperturbed interface ($r = 1$):

$$\left.\begin{aligned} &\tilde{v}_r = s\tilde{u}_r, \quad \tilde{v}_x - 2\Gamma\tilde{u}_r = s\tilde{u}_x, \\ &\tilde{\tau}_{rr} = \tilde{\sigma}_{rr}, \quad \tilde{\tau}_{xr} = \tilde{\sigma}_{xr}. \end{aligned}\right\} \quad (2.12)$$

The term proportional to $\tilde{u}_r$ in the tangential velocity boundary condition represents the variation in the mean velocity of the surface due to the surface displacement.

The equations (2.10) and (2.11) are two fourth-order equations for the velocity field and displacement field respectively. The general solutions for the fluid velocity field are obtained by marching outwards from the centre of the tube. Since two symmetry conditions are applied at the centre of the tube, there are two independent solutions. One of these is determined analytically:

$$\tilde{v}_r^{(1)} = I_1(kr), \quad (2.13)$$

while the other is determined numerically. The general solutions for the displacement field in the wall material are determined by marching inward from the outer surface at $r = H$. Since there are two zero-displacement boundary conditions applied at the outer surface, there are two independent solutions.

2.2. *Numerical method*

The differential equations were solved using a fourth-order Runge–Kutta integrator with adaptive step size control due to the possibility of large variations in the velocity in the viscous wall layer in the high Reynolds number limit. In this limit, the analytical solution (2.13) represents the inviscid 'outer' solution, while the numerically determined solution captures the variation of the velocity field in the wall layer where viscous forces are important. Since only one of the solutions is determined numerically, it is not necessary to use any orthogonalization. There are two general solutions for the displacement field in the solid, both of which are determined by numerically solving the fourth-order equation (2.11). The general solutions for the displacement fields were also determined using a fourth-order Runge–Kutta integrator with adaptive step size control. In addition, it was necessary to use an orthogonalization procedure due to the stiff nature of the equations.

In the solution procedure, the solutions for the fluid velocity and solid displacement fields at the interface are inserted into the boundary conditions (2.12) to obtain a 4×4 characteristic matrix. The determinant of this matrix is set equal to zero to obtain the characteristic equation for the growth rate s. This equation is nonlinear and cannot be reduced to a polynomial in s, so it is not possible to obtain analytical solutions. However, in the viscous limit ($Re = 0$), it was shown by Kumaran (1995*a*) that the characteristic equation reduces to a quadratic equation in the growth rate s, and analytical solutions were obtained in this limit. In the present case, the neutral stability curves at finite Reynolds numbers are determined by numerical continuation using the known solutions at zero Reynolds number as the starting point. In the computations, the wavenumber k is fixed, the real part of the growth rate is set equal to zero ($s_R = 0$) and the Reynolds number is increased in steps of about ($Re/100$). The initial guess for the transition velocity Γ_t and the frequency of the neutrally stable mode $-s_I$ are determined using a predictor–corrector technique, and the Newton–Raphson method is used to obtain the solutions for $-s_I$ and Γ_t at the new Reynolds number.

Two types of verification procedures were used to determine the accuracy of the numerical procedure. The first was to compare the numerical results with previous asymptotic solutions for the growth rate obtained by the author in the high and low Reynolds number limits (Kumaran 1995*a*, *b*). In addition, the results were also compared with numerical solutions of Davey & Drazin (1969) for the stability of fluid flow in a rigid tube. The results of these comparisons are as follows.

(*a*) The comparison with the zero Reynolds number asymptotic analysis of Kumaran (1995*a*) involved setting the Reynolds number equal to zero, while retaining a finite value for the parameter Γ. (Note that the parameter Γ used here is identical to that used in the low Reynolds number analysis of Kumaran 1995*a*.) In this case, it was found that there is exact agreement between the asymptotic and numerical results for the growth rate to within machine precision.

(*b*) The numerical results were compared with the high Reynolds number asymptotic results of Kumaran (1995*b*) for inviscid modes. In that study, the growth rate was determined in the limit $Re \gg 1$ and $(\rho V^2/G) \equiv (\Gamma/Re) \sim 1$. There are multiple solutions for the growth rate, and the solutions were determined using an asymptotic expansion in the small parameter $Re^{-1/2}$. The asymptotic solution is in error by a factor of $O(Re^{-1})$, and the difference between the asymptotic and numerical results should decrease proportional to Re^{-1} in the limit $Re \gg 1$. A comparison between the asymptotic results (s_a) and the numerical results (s_n) for the real and imaginary parts of the growth rates are shown in figure 2(*a*) and figure 2(*b*), while figure 2(*c*) shows $E = (|s_n - s_a|/|s_n|)$, which is the ratio of the magnitude of the error in the asymptotic growth rate and the magnitude of the numerical growth rate. Figures 2(*a*) and 2(*b*) show that there is excellent agreement between the asymptotic and numerical results at Reynolds numbers greater than about 1000. Figure 2(*c*) shows that E decreases proportional to Re^{-1}, as predicted by the asymptotic analysis. In addition, the numerical solutions also exhibit a boundary layer of thickness $Re^{-1/2}$ where viscous effects are important, in agreement with the asymptotic analysis.

(*c*) The results of the present numerical scheme were also compared with previous numerical studies of the linear stability analysis of Davey & Drazin (1969) for the flow in a rigid tube. Davey & Drazin (1969) used two procedures for the solution of the stability equation, a numerical integration procedure and an expansion of the solution in a complete and orthogonal function space, and reported that the agreement between the two techniques is very good. Salwen & Grosch (1972) also

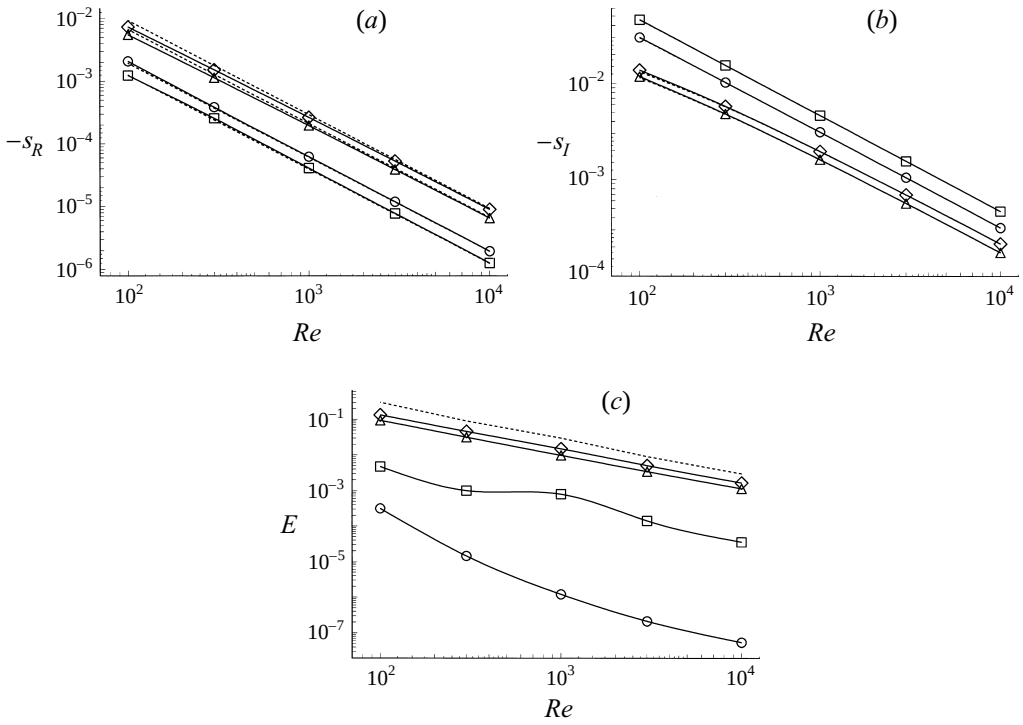

FIGURE 2. A comparison of the numerical results of § 2 with the asymptotic results for the inviscid modes of Kumaran (1995*b*) for $\rho V^2/G = 2$ and $H = 2$: ○, $k = 0.5$, least-damped downstream travelling mode; △, $k = 0.5$, least-damped upstream travelling mode; □, $k = 1.0$, least-damped downstream travelling mode; ◇, $k = 1.0$, least-damped upstream traveling mode. (*a*) Real part of the growth rate s_R as a function of Reynolds number; (*b*) imaginary part of the growth rate s_I as a function of Reynolds number; solid lines are numerical results and broken lines are asymptotic results. (*c*) The ratio $E = (|s_n - s_a|/|s_n|)$; the broken line indicates a slope of -1.

used an expansion in an orthogonal function space and showed that their results are in agreement with those of Davey & Drazin (1972) for axisymmetric perturbations.

Davey & Drazin determined the wave velocities for two different types of modes. The first are the centre modes, where the vorticity is confined to a region of thickness $Re^{-1/4}$ at the centre of the tube, and the second are the wall modes, where the vorticity is confined to a region of thickness $Re^{-1/3}$ at the wall of the tube. The centre modes are not of interest in the present analysis, because the vorticity of these is confined to the centre of the tube, and consequently these are not influenced by the flexibility of the wall. The centre modes cannot be obtained from the present numerical scheme, because the analytic approximation that has been made for one of the linearly independent solutions (2.13) is not appropriate for the centre modes. The wall modes are suitable for comparison with the present analysis, since the wave velocity is likely to be influenced by the wall flexibility, and consequently the results of the present numerical procedure are compared with the wall mode results of Davey & Drazin (1969).

The results of the present numerical technique cannot be directly compared with those for a rigid-walled tube, because there is a fundamental difference in the numerical techniques used. In a flexible tube, the solutions for the fluid velocity field and the displacement field in the wall are obtained by numerical integration procedures start-

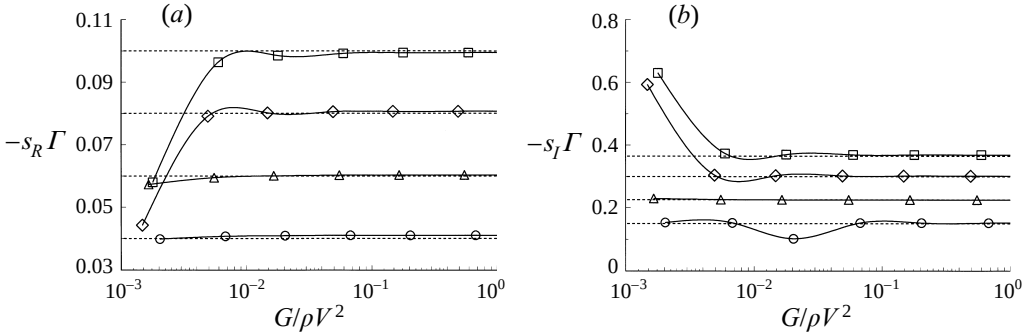

FIGURE 3. A comparison of the numerical results of § 2 (solid lines) for a flexible tube with $H = 2.0$ with the results of Davey & Drazin (1969) (broken lines) for the least-damped mode in a rigid tube. ○, $k = 0.252, Re = 3.22 \times 10^3$; △, $k = 0.563, Re = 6.00 \times 10^3$; □, $k = 1.04, Re = 4.78 \times 10^3$; ◇, $k = 1.00, Re = 8.44 \times 10^3$. (*a*) Real part of s/Γ as a function of $G/\rho V^2$. (*b*) Imaginary part of s/Γ as a function of $G/\rho V^2$.

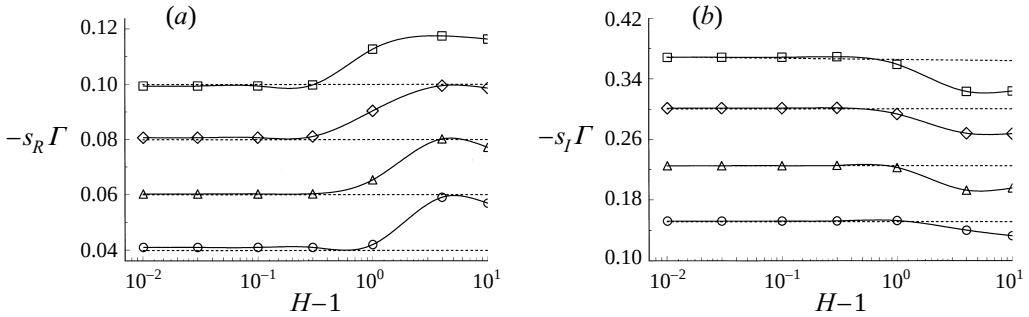

FIGURE 4. A comparison of the numerical results of § 2 (solid lines) for a flexible tube with $G/\rho V^2 = 0.1$ with the results of Davey & Drazin (1969) (broken lines) for the least-damped mode in a rigid tube. ○, $k = 0.252, Re = 3.22 \times 10^3$; △, $k = 0.563, Re = 6.00 \times 10^3$; □, $k = 1.04, Re = 4.78 \times 10^3$; ◇, $k = 1.00, Re = 8.44 \times 10^3$. (*a*) Real part of s/Γ as a function of $H - 1$. (*b*) Imaginary part of s/Γ as a function of $H - 1$.

ing at the centre of the tube and the outer boundary of the wall, and the boundary conditions at the interface are used to obtain the characteristic matrix. In contrast, the numerical procedure for a rigid tube involves a numerical integration from the centre of the tube, followed by a shooting procedure to enforce the boundary conditions at the wall. However, there are two limiting procedures that can be used to compare the present solutions with those for a rigid wall. The first is to take the limit $G \to \infty$ at a fixed value of H, shown in figures 3(*a*) and 3(*b*), and the second is to take the limit $H - 1 \to 0$, at a fixed value of G, shown in figures 4(*a*) and 4(*b*). In these figures, the real and imaginary parts of s/Γ, which is the growth rate scaled by V/R are shown as a function of the parameters $G/\rho V^2$ and $H - 1$. It should be noted that the product s/Γ remains finite even in the limit $G \to \infty$. The values of the wave velocity for a rigid walled channel were extracted from an electronically digitized image of figure 2 of Davey & Drazin (1969), and the error made in determining the numerical values is estimated at 1%. It can be seen from figures 3 and 4 that the flexible-tube solution for the growth rate converges towards the rigid-tube solution in the limit $G/\rho V^2 \gg 1$ and $H - 1 \ll 1$, and the agreement between the present results and those of Davey & Drazin is excellent. Moreover, the numerical calculations show that the

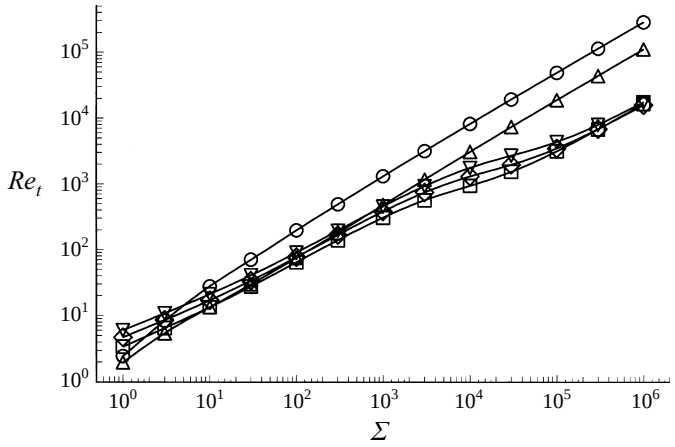

FIGURE 5. The transition Reynolds number, Re_t, as a function of the dimensionless parameter Σ for $H = 2$ and for different values of wavenumber k. ○, $k = 1.0$; △, $k = 2.0$; □, $k = 4.0$; ◇, $k = 6.0$; ∇, $k = 8.0$.

vorticity in the fluid is confined to a boundary layer of thickness $Re^{-1/3}$ at the wall of the tube in the limit of high Reynolds number. This is in qualitative agreement with the asymptotic results of Corcos & Sellars (1959) and the numerical results of Davey & Drazin (1972), confirming that the modes reported here are wall modes.

The above consistency tests indicate that the results of the present analysis are consistent with the previous asymptotic results for a flexible tube, and previous numerical linear stability analyses for a rigid tube.

2.3. *Results*

The transition Reynolds number at which the perturbations become neutrally stable ($s_R = 0$) depends on the wavenumber k, the dimensionless velocity $\Gamma = (V\eta/GR)$, the ratio of wall thickness to tube radius H and the ratio of viscosities η_r. In this section, the behaviour of the transition velocity at $\eta_r = 0$ is first analysed, and then the effect of variation in η_r on the transition velocity is determined. The transition Reynolds number Re_t is shown for $H = 2$, $\eta_r = 0$ and different values of the wavenumber k in figure 5. The abscissa in the graph is chosen to be $\Sigma = Re/\Gamma \equiv \rho GR^2/\eta^2$, since this dimensionless number is independent of the fluid velocity and is a function only of the properties of the fluid and the wall. Figure 5 shows that the transition velocity has a minimum at finite k, indicating that the most unstable modes have finite wavelength.

The critical Reynolds number, which is the minimum Reynolds number at which an instability is predicted, is shown as a function of Σ for different values of H in figure 6(*a*). The critical Reynolds number increases as Σ is increased, and shows a power-law relation of the type $Re_c \propto \Sigma^{\alpha}$ in the limit $\Sigma \gg 1$, where $0.7 < \alpha < 0.75$ for the values of H studied here. The wavenumber of the most unstable mode, k_c, which is shown as a function of Σ in figure 6(*b*), increases on the whole as Σ is increased, and decreases as H is increased. The frequency of the most unstable mode, $-s_{Ic}$, shown in figure 6(*c*), is positive, indicating that the phase velocity of the waves is positive. This is a feature observed for all the neutrally stable modes obtained in the present study.

It is useful to analyse the structure of the fluid velocity field in the limit of high Reynolds number, and compare it with the velocity fields for the inviscid modes. A characteristic feature of a high Reynolds number flow near an oscillatory surface is

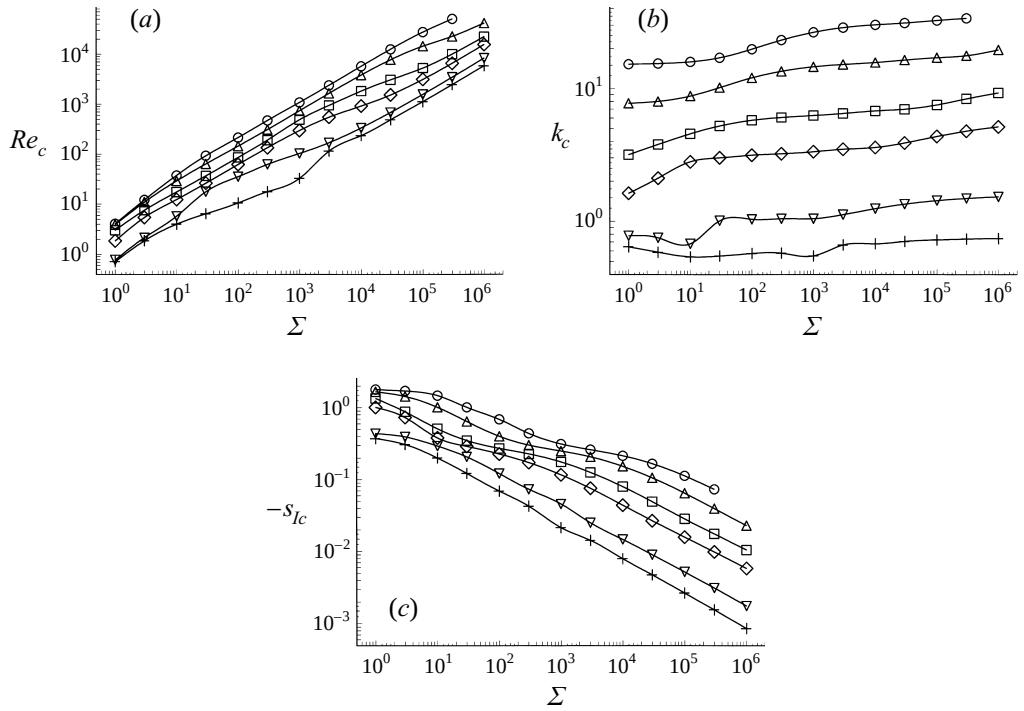

FIGURE 6. The critical Reynolds number Re_c (a), wavenumber of the most unstable mode k_c (b) and frequency of the most unstable mode $-s_{Ic}$ (c) as a function of the parameter Σ for different values of H. ○, $H = 1.1$; △, $H = 1.2$; □, $H = 1.5$; ◇, $H = 2.0$; ∇, $H = 5.0$; +, $H = 10.0$.

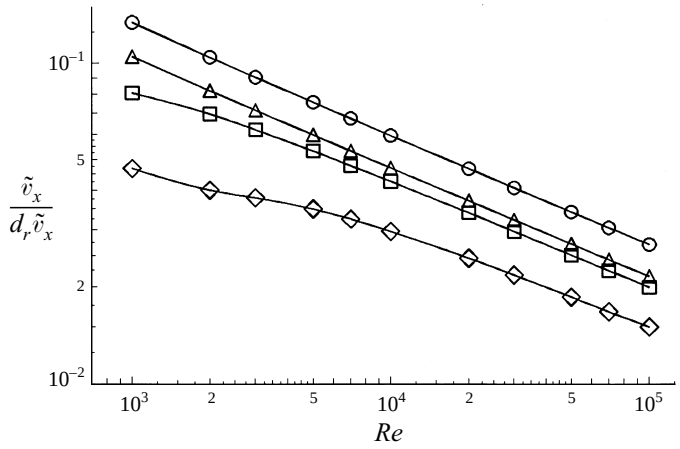

FIGURE 7. The ratio $\tilde{v}_x/d_r\tilde{v}_x$ as a function of Re for neutrally stable modes for $H = 2$. ○, $k = 0.5$; △, $k = 1.0$; □, $k = 3.0$; ◇, $k = 8.0$.

the confinement of the viscous stresses to a small region near the wall of the tube; for further details, the reader is referred to Batchelor (1967). As explained in the previous subsection, the solutions for the fluid velocity profile in the present case can be separated into the outer flow $\tilde{v}_{oi}$ and the wall layer $\tilde{v}_{wi}$, and the ratio $(\tilde{v}_{wx}/d_r\tilde{v}_{wx})$ gives the characteristic wall layer thickness in the present case. This ratio is shown in

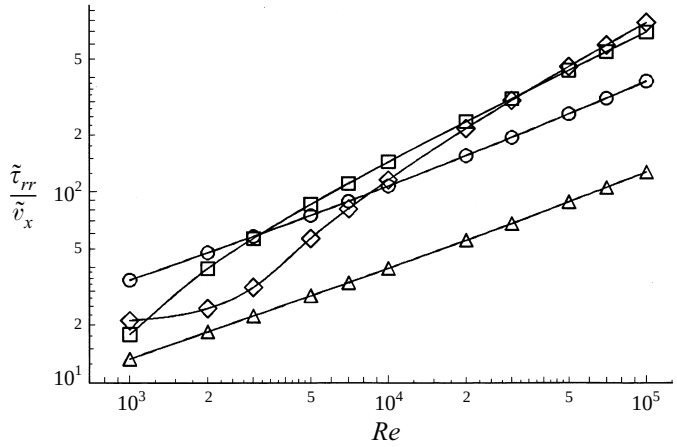

FIGURE 8. The ratio $\tilde{\tau}_{rr}/d_r\tilde{v}_x$ as a function of Re for neutrally stable modes for $H = 2$. ○, $k = 0.5$; △, $k = 1.0$; □, $k = 3.0$; ◇, $k = 8.0$.

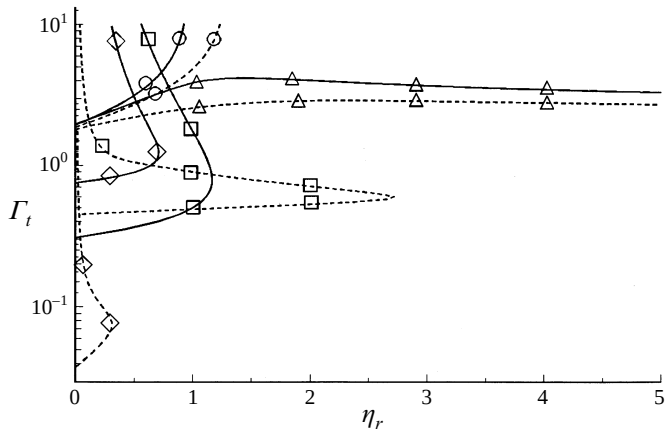

FIGURE 9. The transition value of Γ as a function of η_r for $k = 2$ and $H = 2$ (solid lines) and $H = 10$ (broken lines). ○, $\Sigma = 0.0$; △, $\Sigma = 1.0$; □, $\Sigma = 10^2$; ◇, $\Sigma = 10^4$.

figure 7 for a variation in the transition Reynolds number from 10^3 to 10^5, and for various values of the wavenumber k. The slope of the curve converges to a value of -0.33 in the limit $Re \gg 1$, indicating that the wall layer thickness varies as $Re^{-1/3}$. From figure 7, it can also be inferred that the leading contribution to the ratio of the shear stress and the tangential velocity, $\tilde{\tau}_{xr}/\tilde{v}_x$, due to the flow in the wall layer, scales as $Re^{1/3}$. However, the ratio of the normal stress and the tangential velocity, shown in figure 8, does not show a uniform scaling behaviour that is independent of the wavelength even at $Re = 10^5$, and therefore the instability observed here would not be accessible from asymptotic analysis. This explains why the critical Reynolds number does not show a definite scaling behaviour even at $\Sigma = 10^6$.

The effect of variation in the ratio of viscosities η_r on the stability characteristics is analysed next. In the low Reynolds number analysis of Kumaran (1995*a*), it was found that a variation in the ratio of viscosities causes a qualitative change in the stability characteristics of the system. In this limit, there are unstable modes only when the viscosity η_r is below a maximum value η_{rm} which is a function of H and Σ;

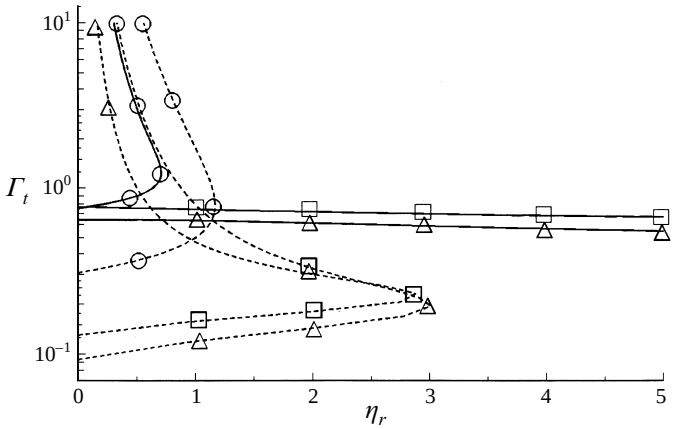

FIGURE 10. The transition value of Γ as a function of η_r for $H = 2$ and $\Sigma = 10^2$ (solid lines) and $\Sigma = 10^4$ (broken lines). ○, $k = 2.0$; △, $k = 4.0$; □, $k = 6.0$.

all perturbations are stable for $\eta_r > \eta_{rm}$ for a given H. In the present case, the effect of variation in the value of the parameter Σ on the neutral stability curves is shown in figure 9. Here, the neutral stability curves are shown in the (Γ, η_r)-plane, and Γ has been chosen as the abscissa in preference to Re so that the case $\Sigma = 0$, where the Reynolds number is zero but the critical value of Γ is non-zero, can be represented. From these curves, it can be seen that there are three distinct types of behaviour at a fixed value of H and wavenumber k.

(i) At $\Sigma = 0$, the instability occurs at a transition value of Γ_t. This transition value increases monotonically as a function of the ratio of viscosities η_r, and diverges at a maximum value η_{rm}. This is in agreement with the low Reynolds number analysis of Kumaran (1995*a*). The divergence of Γ_t is not apparent in figure 9, due to the scale used for the ordinate, but can clearly be seen in Kumaran (1995*a*).

(ii) At $\Sigma = 1$, the transition value of Γ_t initially increases as η_r is increased, reaches a maximum and then decreases when η_r is further increased. The numerical calculations were extended to $\Gamma_t = 10^3$, and it was observed that the value of η_r continued to decrease for the neutrally stable modes.

(iii) At $\Sigma = 10^2$ and $\Sigma = 10^4$, the critical value Γ_t increases as η_r increases and then exhibits a turning point of infinite slope at a maximum value η_{rm}. As the velocity Γ_t is further increased, the ratio of viscosities at which neutrally stable modes are observed decreases, indicating that instabilities can occur only when the ratio of viscosities is less than η_{rm}.

The trends observed in the neutral stability curve depend on the ratio of radii H and the wavenumber k, and are referred to as type (i), (ii) and (iii) behaviour.

The classification of the behaviour of the neutral stability curve given above is specific to a particular value of the wavenumber k. To determine the stability of the system for a given set of fluid and wall properties, and to classify the qualitative behaviour of the neutral stability curve for the most unstable mode, it is necessary to examine the variation in the neutral stability curve as a function of the wavenumber k. The effect of a variation in the neutral stability curves due to a variation in the wavenumber at $H = 2$ is shown in figure 10. The two trends observed in figure 10 at $\Sigma = 10^2$ and $\Sigma = 10^4$, which are typical of the trends observed at other values of Σ as well, are as follows:

(A) At $\Sigma = 10^2$, the neutral stability curve shows type (iii) behaviour, where there

is a turning point at a finite value of η_r, for low values of the wavenumber ($k = 2$). However, at larger values of the wavenumber ($k = 4$ and 6), the neutral stability curves exhibit type (ii) behaviour, where there is very little variation in the transition value Γ_t as a function of η_r. In this case, there is no maximum limit on the ratio of viscosities for the presence of unstable modes.

(B) At $\Sigma = 10^4$, the neutral stability curve shows type (iii) behaviour, where there is a turning point in the Γ_t, Σ curve, at all chosen values of wavenumber. It is further observed that the value of η_r at which there is a turning point first increases and then decreases as the wavenumber is increased. This implies that there is a maximum value η_{rm} at which perturbations with a specific wavenumber are neutrally stable, and there is no instability at any wavenumber when η_r is increased beyond η_{rm}.

The neutral stability curve exhibits Type A behaviour at lower values of Σ, and in this parameter regime there is the possibility of unstable modes at all values of the ratio of viscosities η_r. Type B behaviour is exhibited at higher values of Σ, and in this case it is of interest to find the maximum value of η_{rm} as a function of k for a given set of fluid and wall parameters, since this is the maximum value of ratio of viscosities at which an instability can occur. In order to find the values of Σ where Type A and Type B behaviour are observed, a total of thirteen points which are equidistant on the logarithmic scale in the interval $1 \leqslant \Sigma \leqslant 10^6$ were chosen, and the trends in the neutral stability curve at each of these points was examined to determine whether it belonged to category A or category B. Where it belonged to category B, the maximum value, η^*_{rm}, of the viscosity ratio at which there are neutrally stable modes was evaluated by increasing k in steps of 0.05 from $k = 0$ to $k = 10$ for a given Σ, and evaluating η_{rm} at each value. The interval in which the curve showed a maximum was identified, and the maximum value was obtained by cubic splines. The maximum viscosity η^*_{rm} is shown as a function of Σ in figure 11 in the regions in parameter space in which type B behaviour is observed in the wavenumber interval between 0 and 10. The maximum ratio of viscosities is not shown for $H = 1.2$ and $H = 1.1$ because in these cases, type A behaviour is observed even at $\Sigma = 10^5$. The parameter $\Gamma^*_m = (Re^*_m/\Sigma)$ at which the perturbations become neutrally stable at $\eta_r = \eta^*_{rm}$ is shown as a function of Σ in figure 12. From these figures, it can be inferred that the maximum ratio of viscosities and the Reynolds number for neutrally stable modes at this viscosity ratio increase as Σ increases.

It is useful to compare the results of the present analysis with the experimental observations of Krindel & Silberberg (1979) of the flow in a tube surrounded by a wall made of polyacrylamide gel. The authors measured the flow rate in the tube at a fixed pressure drop, and compared it with the expected flow rate if the flow were in the laminar regime. In a rigid tube, the flow rate showed a discontinuous decrease at a Reynolds number of about 2100 where the laminar to turbulent transition might be expected. In the gel-walled tube, however, the authors reported that the flow rate was significantly lower than that for a laminar flow in a rigid tube even at a Reynolds number of about 800. (Note that the Reynolds number defined here based on the radius and maximum velocity is identical to that used in tube flow literature based on the diameter and mean velocity.) An attempt was made to observe the onset of turbulence by the injection of a dye stream into the tube. The authors reported that the dye stream in the centre of the tube becomes chaotic at a Reynolds number between 570 and 870. However, the authors cautioned that this might overestimate the transition Reynolds number since the turbulence appears to originate at the walls and then grows inwards to engulf the laminar core.

The parameters Σ and H can be evaluated from the data provided by them, but

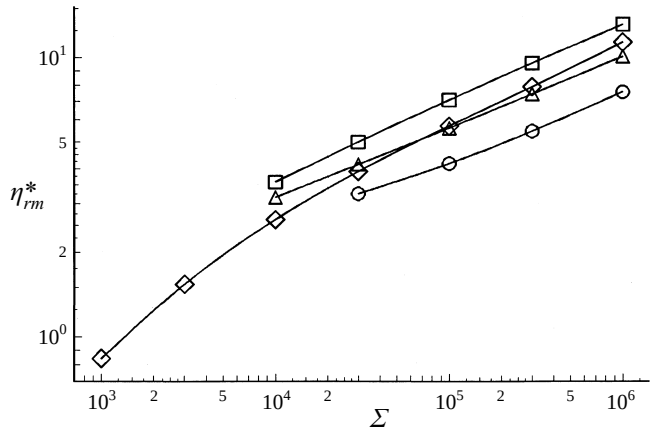

FIGURE 11. The maximum value of the viscosity ratio, η^*_{rm}, at which neutrally stable modes can exist, as a function of Σ. ○, $H = 1.5$; △, $H = 2.0$; □, $H = 5.0$; ◇, $H = 10.0$.

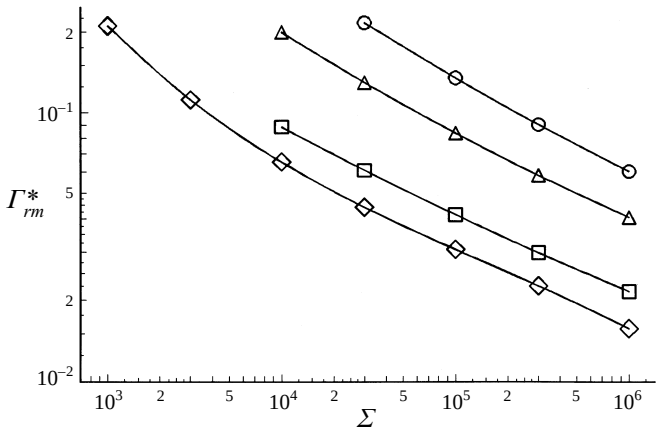

FIGURE 12. The parameter $\Gamma^*_m = Re^*_m/\Sigma$ at which perturbations become neutrally stable at the maximum ratio of viscosities, as a function of Σ. ○, $H = 1.5$; △, $H = 2.0$; □, $H = 5.0$; ◇, $H = 10.0$.

H	Σ	Re_c (at $\eta_r = 0$)	k_c (at $\eta_r = 0$)	η^*_{rm}	Re^*_m	ω
9.67	8.201×10^3	209.30	0.667	2.42	579.41	-7.886×10^{-3}
9.67	3.076×10^4	480.09	0.705	7.90	675.72	-4.04×10^{-3}
31.0	3.076×10^4	310.28	0.775	10.03	404.14	-3.28×10^{-3}

TABLE 1. The critical Reynolds number and wavenumber at $\eta_r = 0$, and the maximum viscosity η^*_{rm} and Reynolds number Re^*_{rm}, for the experiments of Krindel & Silberberg (1979)

it is not possible to obtain the ratio of viscosities η_r since the loss modulus (which is the complex part of the shear modulus) was not reported in their experiments. The loss modulus in a gel is sensitive not only to the concentration, but also to the pH and the degree of cross-linking in the gel (Schosseler, Ilmain & Candau 1991). Since these other parameters were not reported by Krindel & Silberberg, the loss modulus cannot be easily estimated from their experimental data. Therefore,

the critical Reynolds number at $\eta_r = 0$ (which represents the lower limit, since the critical Reynolds number at $\eta_r > 0$ is greater) is given in table 1. In addition, the Reynolds number of the neutrally stable modes at the maximum viscosity ratio η_{rm} is also compared with their analysis using a reasonable estimate of the ratio of loss and storage moduli. The viscosity ratio can be estimated as $\eta_r = (G''/G')|\omega|^{-1}$, where G' and G'' are the storage and loss moduli, and the frequency ω has been scaled by G'/η. The ratio of moduli (G''/G') is between 0.01 and 0.1 for most polymeric gels (see, for example, the results of Tong & Liu 1993). Using the value of ω for the neutrally stable perturbations, this corresponds to a viscosity ratio between 1.268 and 12.68 for case (i), between 2.475 and 24.75 for case (ii), and between and 3.05 and 30.49 for case (iii). In all the three cases, the maximum viscosity ratio predicted by the analysis is greater than the lower limit, but less than the upper limit. A more definite evaluation of the results cannot be made owing to a lack of data, but the comparison indicates that the instability observed by Krindel & Silberberg could be the same as that predicted by the analysis if the ratio of moduli is closer to 0.01.

3. Conclusions

The present numerical study of the stability of the fluid flow in a flexible tube in the intermediate Reynolds number regime complements the earlier low and high Reynolds number asymptotic analyses (Kumaran 1995*a*, *b*), and provides the stability characteristics over a range of Reynolds numbers $1 < Re < 10^4$. The stability characteristics for the case $\eta_r = 0$ were studied first. The results indicate that the flow becomes unstable when the Reynolds number is increased beyond a critical value for all values of Σ in the range $1 < \Sigma < 10^6$, and the critical Reynolds number increases with Σ. In the limit of high Reynolds number, the critical Reynolds number increases as Σ^{α}, where α has a value between 0.7 and 0.75 for the values of H studied here. This range of scaling exponents is higher than that for the stable inviscid modes (Kumaran 1995*b*), for which $Re \sim \Sigma^{1/2}$. In addition, the boundary layer thickness in the limit $Re \gg 1$ decreases proportional to $Re^{-1/3}$, in contrast to the decrease proportional to $Re^{-1/2}$ for the inviscid modes. These results indicate that the mode that becomes unstable in the present analysis is different from the inviscid modes studied in Kumaran (1995*b*).

The reason for the difference in the boundary layer scaling is briefly discussed here; a more detailed asymptotic analysis in the parameter regime $Re \sim \Sigma^{3/5}$ is given in a future publication (Kumaran 1998). That scaling analysis for the wall modes shows that the vorticity is confined to a boundary layer of thickness $Re^{-1/3}R$ near the wall, and it is convenient to define a scaled coordinate $z^{\dagger} = Re^{1/3}(1 - r^*)/R$, where r^* is the dimensional distance perpendicular to the flexible wall. The growth rate of the wall modes is $O(Re^{-1/3})$ smaller than the strain rate in the fluid, and the appropriate scaled growth rate is $s^{\dagger} = Re^{1/3}(s^*R/V)$, where s^* is the dimensional growth rate of the perturbations. In addition, the continuity equation indicates that the velocity normal to the wall is $O(Re^{-1/3})$ smaller than the tangential velocity, and if the scaled tangential velocity is defined as $\tilde{v}_x^{\dagger} = \tilde{v}_x^*/V$, the scaled normal velocity is $\tilde{v}_r^{\dagger} = Re^{1/3}\tilde{v}_r^*/V$, where $\tilde{v}_x^*$ and $\tilde{v}_r^*$ are dimensional velocities. The leading-order Navier–Stokes equations in the limit $Re \gg 1$, expressed in terms of these scaled variables, are

$$d_{z^{\dagger}}\tilde{v}_r^{\dagger} + \mathrm{i}k^{\dagger}\tilde{v}_x^{\dagger} = 0, \tag{3.1}$$

$$d_{z^{\dagger}}\tilde{p}^{\dagger} = 0, \tag{3.2}$$

$$-\mathrm{i}k^{\dagger}\tilde{p}^{\dagger} + [-(s^{\dagger} + \mathrm{i}k^{\dagger}z^{\dagger}) + d_{z^{\dagger}}^2]\tilde{v}_x^{\dagger} = 0, \tag{3.3}$$

where $k^\dagger = kR$ and $\tilde{p}^\dagger = \tilde{p}^*/(Re^{-1/3}\rho V^2)$ are the scaled wavenumber and pressure. The above equations can be solved analytically, but it is sufficient to examine these equations to obtain some physical insight into the structure of the wall modes. It can be seen that the tangential velocity at the wall is large compared to the normal velocity, and the velocity in the flow is driven by the velocity in the boundary layer. This is in contrast to the inviscid modes, where the flow in the boundary layer is driven by the inviscid flow in the bulk of the fluid. In addition, equation (3.3) also shows that the viscous effect (given by the second spatial derivative of the tangential velocity) is of the same magnitude as the inertial terms, in contrast to the inviscid modes where the viscous effects are $O(Re^{-1/2})$ smaller than the inertial effects. Consequently, the instability is caused by modes that are distinct from the inviscid modes, and this explains why the present instability was not observed in the asymptotic analysis of Kumaran (1995*b*). Though the boundary layer for the fluid velocity field exhibits a clear scaling behaviour, no similar scaling behaviour was observed for the displacement field in the wall material. The present parameter regime cannot be accessed by asymptotic analysis, because unstable modes are found for $Re \propto \Sigma^{0.7}$, which is different from the regime $Re \propto \Sigma^{3/5}$ for the asymptotic analysis. In addition, it should be noted that the asymptotic analysis of the wall modes (Kumaran 1998) does not indicate the presence of an instability, and the present instability has to be interpreted as a continuation of the wall modes into the intermediate Reynolds number regime where the asymptotic analysis is no longer valid.

The physical mechanism leading to the instability can be explained using an energy balance analysis (Kumaran 1995*b*). A balance for the total energy of the fluctuations can be written as

$$\frac{\mathrm{d}\mathscr{E}}{\mathrm{d}t} = \mathscr{C} + \mathscr{S} - \mathscr{D}_f - \mathscr{D}_w \tag{3.4}$$

where $\mathscr{E}$ is the energy of the fluctuations, $\mathscr{C}$ is the rate of transfer of energy from the mean flow to the fluctuations due to the convective terms in the momentum equation, $\mathscr{S}$ is the transfer of energy due to the work done by the mean flow at the interface, and $\mathscr{D}_f$ and $\mathscr{D}_w$ are the rates of dissipation of energy due to viscous effects in the fluid and the wall. In the leading approximation, the convective transport of energy $\mathscr{C}$ is zero because the tangential and normal velocities in the fluid are out of phase by an angle of $\pi/2$ (Kumaran 1995*b*). Thus, there is an instability when the energy transfer rate $\mathscr{S}$ is larger than the rate of dissipation $\mathscr{D}_f + \mathscr{D}_w$. The rate of transport due to the work done by the mean flow at the interface is

$$\mathscr{S} = 2\pi R \int \mathrm{d}x^* \tau^*_{xr}(v^*_x - \partial_{t^*} u^*_x)|_{r^*=R} \tag{3.5}$$

where * is used to denote dimensional quantities. The rate of dissipation of energy in the fluid is

$$\mathscr{D}_f = 2\pi\eta \int \mathrm{d}x^* \int_0^R r^* \,\mathrm{d}r^* \, \tau^*_{xr}(\partial_{r^*} v^*_x + \partial_{x^*} v^*_r). \tag{3.6}$$

From the scaling of the spatial and velocity coordinates in equations (3.1) to (3.3), it can be inferred that the tangential velocity v^*_x is large compared to the normal velocity in the wall layer. In addition, the tangential velocity v^*_x is also large compared to the rate of change of normal displacement $\partial_{t^*} u^*_x$ in (3.5); in the leading approximation, $\tilde{v}_x$ is balanced by the term proportional to $2\Gamma\tilde{u}_r$ in the tangential velocity boundary condition (2.12). With these simplifications, $\mathscr{S}$ can be expressed in terms of the Fourier

components of the velocities $\tilde{v}_r$ and $\tilde{v}_x$:

$$\mathscr{S} = (Re^{1/3} 2\pi R\eta V^2) \exp[(s^\dagger + \bar{s}^\dagger)] \int \mathrm{d}k^\dagger [\bar{\tilde{v}}_x^\dagger d_{z^\dagger} \tilde{v}_x + \tilde{v}_x^\dagger d_{z^\dagger} \bar{\tilde{v}}_x^\dagger]|_{r=1} \tag{3.7}$$

where the overbar denotes the complex conjugate. The rate of dissipation of energy in the fluid can be expressed in a similar fashion:

$$\mathscr{D}_f = (Re^{1/3} 2\pi R\eta V^2) \exp[(s^\dagger + \bar{s}^\dagger)] \int \mathrm{d}k^\dagger \int_0^\infty \mathrm{d}z^\dagger [2(d_{z^\dagger} \tilde{v}_x^\dagger)(d_{z^\dagger} \bar{\tilde{v}}_x^\dagger)]. \tag{3.8}$$

In the above expression, the lower limit $z^\dagger = 0$ corresponds to the wall of the tube, while the upper limit $z^\dagger = Re^{1/3}$ at the centre of the tube has been approximated by $z^\dagger = \infty$ in the limit $Re \gg 1$. The difference $\mathscr{S} - \mathscr{D}_f$ reduces to

$$\mathscr{S} - \mathscr{D}_f = (Re^{1/3} 2\pi R\eta V^2) \exp[(s^\dagger + \bar{s}^\dagger)] \int \mathrm{d}k^\dagger \int_0^\infty \mathrm{d}z^\dagger [(\bar{\tilde{v}}_x^\dagger d_{z^\dagger}^2 \tilde{v}_x^\dagger) + (\tilde{v}_x^\dagger d_{z^\dagger}^2 \bar{\tilde{v}}_x^\dagger)]. \tag{3.9}$$

For a non-dissipative wall ($\eta_r = 0$), there is a transition from stable to unstable modes when $\mathscr{S} - \mathscr{D}_f$ goes from negative to positive. Therefore, there is an instability when the transfer of energy from the mean flow to the fluctuations due to the shear work done at the surface is larger than the rate of dissipation of energy in the fluid for a non-dissipative wall.

The effect of variation in η_r on the stability was analysed, and it was found that a variation in η_r could qualitatively alter the stability characteristics; these are summarized in § 2. It is found that wall dissipation could either stabilize or destabilize the flow, depending on the parameter regime under consideration. The physical reason for the stabilization or destabilization of the fluctuations has been explained in the classic papers of Landahl (1962) and Benjamin (1963). However, the present analysis reveals that the wall viscosity could have a complex effect on the stability, and it is found that for some ranges of Σ, there is a maximum viscosity ratio beyond which unstable modes do not exist. A similar observation regarding the extreme sensitivity of the neutral stability curves to the damping in the elastic surface has been made by Gajjar & Sibanda (1996) in their asymptotic analysis of the flow in a channel with compliant boundaries.

The unstable modes observed here come under the category of Flow Induced Surface Instability in the classification scheme of Carpenter & Garrad (1985), and are distinct from the Tollmien–Schlichting modes which can exist in flows past rigid surfaces. However, it is difficult to classify these modes using the scheme of Benjamin (1963) based on the effect of wall damping on the stability of the system, because an increase in wall viscosity could stabilize or destabilize the perturbations depending on the value of Σ.

The results indicate that the flow in a flexible tube could become unstable at Reynolds numbers that are significantly lower (sometimes an order of magnitude lower) than the transition value of 2100 for a rigid tube. This finding is in qualitative agreement with the experimental results of Krindel & Silberberg (1979), who reported that the drag force in a gel-walled tube is significantly higher than that in a rigid tube at Reynolds numbers as low as 800, and that the flow in the tube becomes turbulent at a Reynolds number as low as 570. A quantitative comparison between the experimental and theoretical results could not be made, because the ratio of viscosities η_r could not be determined from the data provided by Krindel & Silberberg. However, the lower limit of the critical Reynolds number, which corresponds to $\eta_r = 0$, is lower than the transition Reynolds number reported by Krindel & Silberberg. In addition,

an estimate of the ratio of viscosities was obtained using a reasonable estimate of the ratio of the storage and loss moduli for swollen polymer gels. The maximum ratio of viscosities predicted by the present analysis was within the estimated range of viscosity ratios, indicating that the high drag force observed by Krindel & Silberberg could be due to the instability predicted here. However, further experiments are necessary for more detailed comparisons.

The author would like to thank the Department of Science and Technology, Government of India for financial support.

REFERENCES

Batchelor, G. K. 1967 *An Introduction to Fluid Dynamics*. Cambridge University Press.

Benjamin, T. B. 1963 The threefold classification of unstable disturbances in flexible surfaces bounding inviscid flows. *J. Fluid Mech.* **16**, 436–450.

Bertram, C. D. 1986 Unstable equilibrium behaviour of collapsible tubes. *J. Biomech.* **19**, 61.

Bertram, C. D., Raymond, C. J. & Peldey, T. J. 1989 Mapping or instabilities during flow through collapsible tubes. *J. Fluids Struct.* **4**, 125–154.

Carpenter, P. W. & Garrad, A. D. 1985 The hydrodynamic stability of flows over Kramer-type compliant surfaces. Part 1. Tollmien–Schlichting instabilities. *J. Fluid Mech.* **155**, 465–510.

Corcos, G. M. & Sellars, J. R. 1959 On the stability of fully developed pipe flow. *J. Fluid Mech.* **5**, 97–112.

Davey, A. & Drazin, P. G. 1969 The stability of Poiseuille flow in a pipe. *J. Fluid Mech.* **36**, 209–218.

Gajjar, J. S. B. & Sibanda, P. 1996 The hydrodynamic stability of channel flow with compliant boundaries. *Theor. Comput. Fluid Mech.* **8**, 105–129.

Garg, V. K. & Rouleau, W. T. 1972 Linear spatial stability of pipe Poiseuille flow. *J. Fluid Mech.* **54**, 113–127.

Gill, A. E. 1965 On the behavior of small disturbances to Poiseuille flow in a circular pipe. *J. Fluid Mech.* **21**, 145–172.

Harden, J. L., Pleiner, H. & Pincus, P. A. 1991 Hydrodynamic surface modes on concentrated polymer solutions and gels. *J. Chem. Phys.* **94**, 5208–5221.

Jensen, O. E. & Pedley, T. J. 1989 The existence of steady flow in a collapsed tube. *J. Fluid Mech.* **206**, 339–374.

Krindel, P. & Silberberg A. 1979 Flow through gel-walled tubes. *J. Colloid Interface Sci.* **71**, 34–50.

Kumaran, V. 1993 Surface modes on a polymer gel of finite thickness. *J. Chem. Phys.* **98**, 3429–3438.

Kumaran, V. 1995*a* Stability of the viscous flow of a fluid through a flexible tube. *J. Fluid Mech.* **294**, 259–281.

Kumaran, V. 1995*b* Stability of the flow of a fluid through a flexible tube at high Reynolds number. *J. Fluid Mech.* **302**, 117–139.

Kumaran, V. 1996 Stability of inviscid modes in a flexible tube. *J. Fluid Mech.* **320**, 1–17.

Kumaran, V. 1998 Stability of wall modes in a flexible tube. *J. Fluid Mech.* (in press).

Landahl, M. T. 1962 On the stability of a laminar incompressible boundary layer over flexible surface. *J. Fluid Mech.* **13**, 609–632.

Landau, L. D. & Lifshitz, E. M. 1989 *Theory of Elasticity*. Pergamon.

Reyn, J. W. 1987 Multiple solutions and flow limitation for steady flow through a collapsible tube held by open ends. *J. Fluid Mech.* **174**, 467–493.

Salwen, H. & Grosch, C. E. 1972 The stability of Poiseuille flow in a pipe of circular cross section. *J. Fluid Mech.* **54**, 93–112.

Schosseler, F., Ilmain, F. & Candau, S. J. 1991 Structure and properties of partially neutralized poly(acrylic acid) gels. *Macromolecules* **24**, 225–234.

Tong, Z. & Liu, X. 1993 Dynamic mechanical behavior or polyelectrolyte gels with sulfonic acid groups. *Macromolecules* **26**, 4964–4966.